Received: 7 April 2022 | Revised: 22 July 2022 | Accepted: 3 August 2022

DOI: 10.1002/ppap.202200066

RESEARCH ARTICLE

PLASMA PROCESSES AND POLYMERS

Quantitative measurement of NO_2^- distribution in plasma jet treated model tissue, based on image processing technology

Bingkai Wang[1] | **Huaiji Wang**[2] | **Yuqi Wang**[1] | **Yuhan Li**[1] | **Xiang Mao**[2] | **Zilan Xiong**[1]

[1]State Key Laboratory of Advanced Electromagnetic Engineering and Technology, Huazhong University of Science and Technology, Wuhan, Hubei, People's Republic of China

[2]Institute of Environmental Health, Wuhan Center for Disease Control and Prevention, Wuhan, People's Republic of China

Correspondence

Zilan Xiong, State Key Laboratory of Advanced Electromagnetic Engineering and Technology, Huazhong University of Science and Technology, Wuhan, Hubei 430074, People's Republic of China.
Email: zilanxiong@hust.edu.cn

Xiang Mao, Institute of Environmental Health, Wuhan Center for Disease Control and Prevention, Wuhan 430024, People's Republic of China.
Email: maox@whcdc.org

Funding information

National Natural Science Foundation of China, Grant/Award Number: 51907076; Institute of Environmental Health, Wuhan Center for Disease Control and Prevention

Abstract

One of the key issues in plasma medicine is the measurement of the spatial-temporal distribution and total amount of reactive species in treated tissue. Here, we provide a solution based on image processing technology. A DC-driven air plasma jet was used, and NO_2^- was selected as the representative for the test. The model tissue was frozen sliced, and the relationship between the color and standard concentration was established. The temporal distributions of NO_2^- concentration versus time and flow rate were analyzed in each slice, and the total amount of NO_2^- in the treated tissue was obtained. This study offers a new diagnostic method for reactive species amount into tissue, which is an effective guide for plasma medicine applications and numerical modeling research.

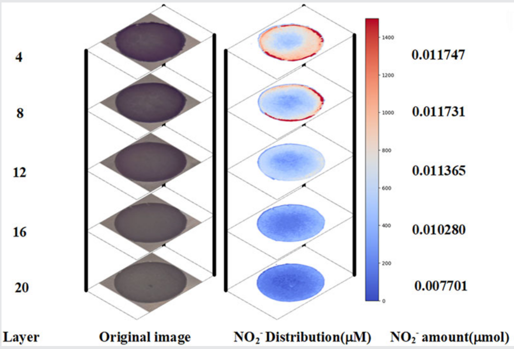

KEYWORDS

absolute amount, model tissue, NO_2^- concentration, plasma jet, spatial distribution

1 | INTRODUCTION

Cold atmospheric plasma has been widely used in the biomedical field, such as in dermatological,[1-3] cardiovascular, and neurological diseases.[4] The mechanism of interaction of plasma with tissues remains a research hotspot worldwide. It is widely accepted that reactive nitrogen species (RNS) and reactive oxygen species (ROS) play an important role in the treatment process,[5] including long-lived species, such as NO_2^-, NO_3^-, H_2O_2, and O_3, and short-lived species, such as O and OH. During plasma treatment of biological tissues, the reactive composition of plasma leads to penetration, uptake, and chemical reactions with tissues. Understanding the interaction between plasma and tissue is important and necessary. Due to the complex

---

Bingkai Wang and Huaiji Wang contributed equally to this study.

characteristics of the treated tissue and limited diagnostic methods, it is difficult to achieve an accurate spatial distribution diagnosis of species concentration inside the tissue, which is one of the key problems in explaining the relationship between reactive oxygen and nitrogen species (RONS) dose and treatment effect.[6]

To facilitate these studies, gelatin[7] or agarose[8] models are used to replace real human tissues. Gelatin models use animal tissue extracts, which have many similarities to human tissues in terms of composition and structure. At present, the diagnosis of RONS inside the treated tissue is mainly a qualitative approach. Color-forming reactions, such as KI-starch and Griess, can indicate the distribution and relative amount of RONS. Omran et al. used a He+O_2 jet to treat uniformly mixed KI-starch agar models, and the oxidation of ROS caused starch to turn blue. In the direction of the centerline of the petri dish, the color depth exhibited a parabolic shape that increased and then decreased, corresponding to the amount of ROS penetration.[9] A similar method was used to detect H_2O_2.[10] Kawasaki et al. used different structures of gelatin and agar models to simulate different human tissues and mixed KI-starch as detection reagents and visualized the ROS distribution in two-dimensional planes by measuring the absorbance at fixed points.[11–15] These two-dimensional images cannot reflect the spatial distribution of ROS inside the model tissue, and the spatial distribution of the concentration cannot be obtained.

To obtain the distribution inside the treated tissue, He et al. used He+O_2 and Ar+O_2 jets to treat gelatin models mixed with KI-starch and sliced every layer of the gelatin using a freezing microtome. The spatial distribution of the infiltrated ROS was qualitatively characterized by comparing the color change of each layer of the section images and the effect of different angles and carrier gases on the processing range.[16,17] Using color-forming reactions, the distribution characteristics of RONS in tissues were qualitatively analyzed, including two-dimensional shape and three-dimensional spatial characteristics. The concentration characteristics of the RONS distribution could be qualitatively analyzed by the color depth, which has some reference significance for the treatment condition (treatment time, distance, angle, etc.) in plasma medicine applications. However, it still could not quantitatively explain the relationship among the treatment conditions, RONS amount, and treatment effect on human tissues.

The quantitative diagnostic approach for RONS penetration is mainly the measurement of penetration depth or transformation into indirect liquid phase measurements, mainly through UV-Vis spectroscopy. He et al. used SMD to treat gelatin mixed with Griess and found that NO_2^- penetrated uniformly on the surface and showed an increasing trend in penetration depth with increasing time.[18] In addition, the penetration depth of RONS along the radial direction under jet treatment was measured by microscopy.[16,17] Nie et al. treated isolated animal tissues with a He+O_2 jet and ground the treated tissues in a buffer such that the reactive species were uniformly mixed into the buffer. They then measured the RONS concentration in a liquid buffer.[19–21] The quantitative diagnostic objects in the above methods mainly target the depth of penetration without being able to obtain the amount and spatial distribution characteristics of the RONS concentration, and the conversion to liquid-phase diagnostics can only approximate the overall average concentration of RONS in a piece of tissue. In addition to UV-Vis, mass spectrometry imaging, as a method to accurately measure the composition of single-layer sections, is targeted for laser scanning diagnostics to measure small-molecule metabolites, lipids, proteins, and pharmaceutical compounds. It has high accuracy and reliable results, and can quantitatively obtain spatial distribution characteristics[22,23]; however, this method mainly measures organic substances and is extremely expensive.

None of the existing diagnostic schemes can quantitatively diagnose the spatial distribution of RONS concentration inside plasma-treated tissue. Digital image processing has great potential as a measurement technology. Qualitative or quantitative measurement of the concentration can be achieved by analyzing the relationship between the color characteristics of the image and the concentration parameter. Nakano et al. proposed red, green, blue (RGB)-based oximetry to assess the ocular fundus and determine its oxygen saturation (SO2) and hemoglobin concentration.[22] Image processing technology has also been used in plasma diagnosis in recent years, but the limited literature mainly focuses on determining the characteristics of the discharge, for example, the discharge type and discharge homogeneity.[23–25] Our latest work investigated the visible light information of surface microdischarges and developed a method to recognize the operation mode based on a gray-level histogram.[26]

In our previous study, a low-cost solution for the accurate measurement of liquid-phase NO_2^- in plasma-active water was proposed based on image-processing technology.[27] However, this method is suitable for liquid-phase products with uniform distribution and therefore cannot be used to measure a nonuniform distribution in the solid phase. In this study, we further investigated the spatial distribution and quantitative measurement of NO_2^- concentrations in plasma-treated tissues and proposed a fast, low-cost, and accurate method based on image processing technology. A gelatin-polysaccharide model has been used.[28,29] A DC-driven air plasma jet was used to treat the model tissue with a chromogenic agent, and NO_2^{-} was selected as the representative for the test. The RGB and hue, saturation and value (HSV) color information of the treated sample was taken from the images, and a segmented linear equation between the color and standard concentration was built. Thereafter, the concentration at each point in each layer of the plasma-treated model tissues was obtained. The penetration depth was measured using morphological imaging operations. Finally, the total absolute amount of NO_2^{-} was determined.

2 | EXPERIMENTAL METHODS AND MATERIALS

2.1 | Sample preparation

During the plasma treatment of human tissues, NO_2^{-} (one of the main RNS species in the aqueous phase) was produced. NO_2^{-} was detected using Griess reagent.[30] The degree of color varies with different NO_2^{-} concentrations, and thus the quantitative relationship between concentration and color can be obtained by using a standard concentration of NO_2^{-} with specific data analysis.

As shown in Figure 1, 15% gelatin (Sigma–Aldrich) and 2% starch (Sinopharm) were prepared as model tissues and mixed with Griess (0.68% sulfonamide, Sinopharm; 0.21% N-naphthyl-ethylenediamine, Sinopharm; 1.39% citric acid, Sinopharm; with a theoretical detectable NO_2^{-} concentration of 4000 μM). A $NaNO_2$ (Sinopharm) solution was added to the model tissue solution and stirred until the color was uniform to generate a model tissue with a range of standard NO_2^{-} concentrations (0, 50, 100, 150, 200, 400, 600, 800, 1000, 1500, 2000, and 3000 μM). The model tissue was then poured into a ϕ22 mm petri dish for solidification. The model tissue was frozen at −20°C using a freezing microtome (Leica, CM 1950) for 20 min and then sliced into 100 μm per piece for pictures taken by a camera (NIKON). We acquired five measurement images at each standard concentration for processing with the OpenCV Python library because pixel values varied considerably with different concentrations. The average values of the five measurements at each concentration were then used to conduct data analysis to ensure the reliability of the results.

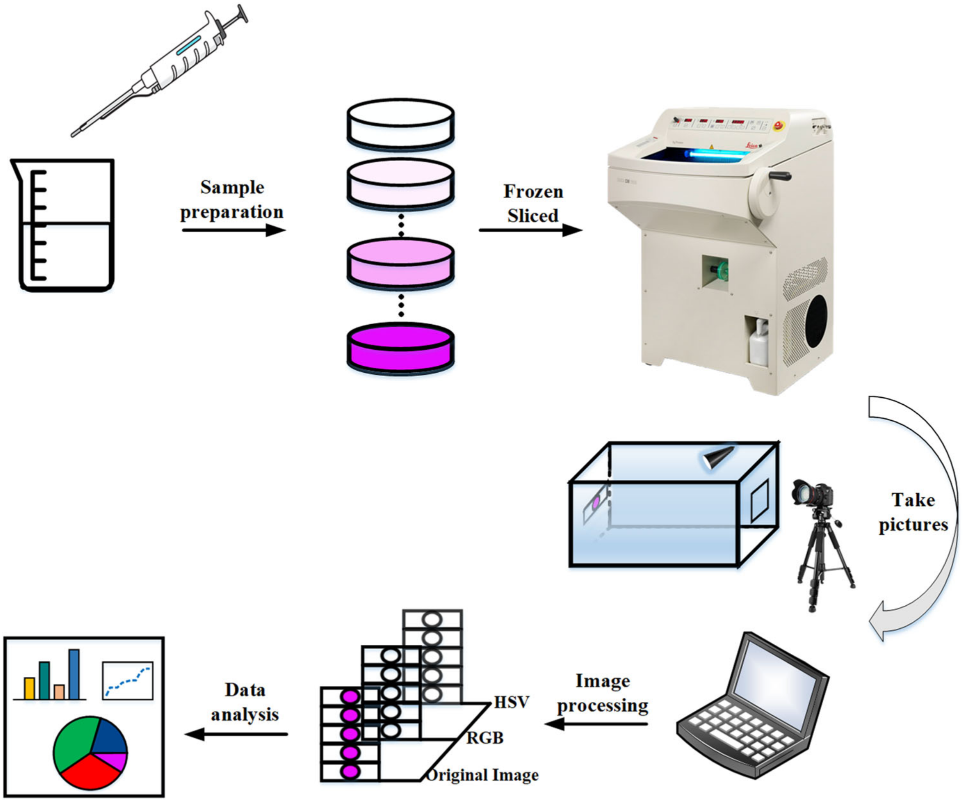

FIGURE 1 General procedure of the proposed method

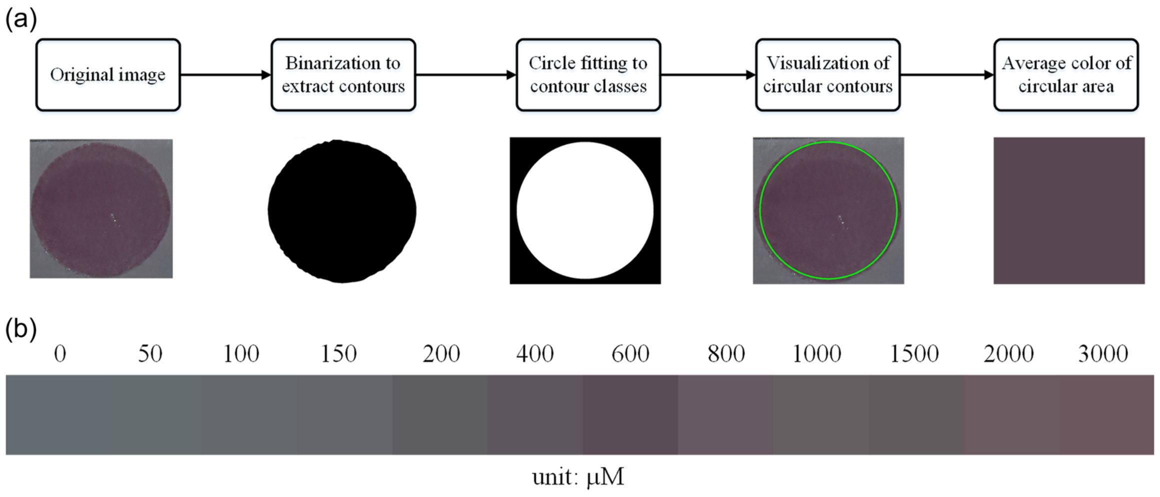

FIGURE 2 Extraction flow of mean color. (a) Image processing for the average pixel of the slice area. (b) The mean color of each standard concentration.

2.2 | Corresponding scheme and measurement of spatial distribution

As different degrees of the chromogenic reaction occurred at different concentrations of NO_2^-, the relationship between the image color and concentration could be analyzed. The average color of the slice area was obtained using digital image processing, as shown in Figure 2a. First, the original image was converted into a gray image, and Ostu binarization was used to extract the contours. Second, we conducted circle fitting and visualized circular contours. Finally, the average color of the circular area was obtained. As shown in Figure 2b, the average color of each standard concentration could be obtained, and then multivariate linear or nonlinear fitting could be used to obtain a continuous relationship curve between color and concentration.

The average color can be expressed in terms of pixel values (R, G, B) or (H, S, V). As shown in Figure 2b, as the concentration increased, the color did not deepen gradually but became lighter and then darker after 800 μM. Because of the presence of saturation precipitation at higher NO_2^- concentrations, this leads to uneven color distribution. In the image color space, it is possible to find pixel values that are consistent with the trend of concentration to facilitate the fitting with concentration. The RGB values partially fluctuate with concentration, but the H value in the HSV color space always maintains an increasing trend. As shown in Figure 3, the NO_2^- concentration increased approximately linearly when the H value varied in the range of 100–160. At H values greater than 160, the increasing trend is still maintained, but the slope increases. To achieve a more accurate concentration calculation, it is not sufficient to perform concentration fitting using only the H value. Therefore, a multivariate linear fit with the RGB values, which have a higher correlation with the concentration, is considered as the segmentation condition with the H value.

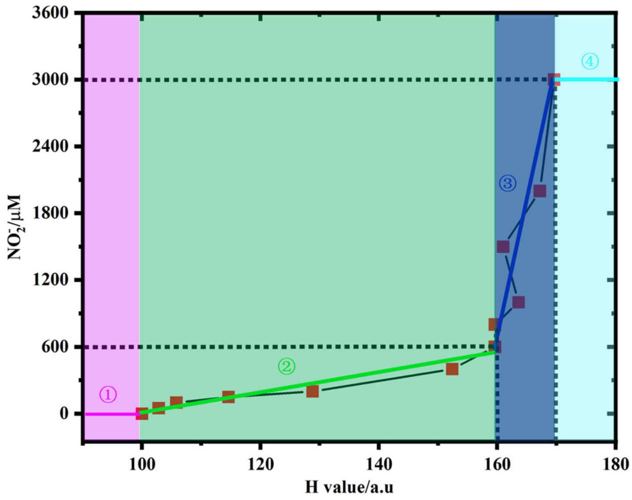

FIGURE 3 NO_2^- concentrations with H value, and the H value was used as the segmentation condition to divide the RGB-concentration fitting into four segments of ①②③④

Based on Figure 3, we divided the segmented linear fit into four segments based on the H value, with the RGB values as the fitted independent variables and NO_2^- concentration C(μm) as the dependent variable.

①When H was less than 100, the concentration was 0, as given in Equation (1):

$$C_1 = 0. \tag{1}$$

②When H was greater than 100 and less than 160, a multivariate linear fit of the standard concentration was

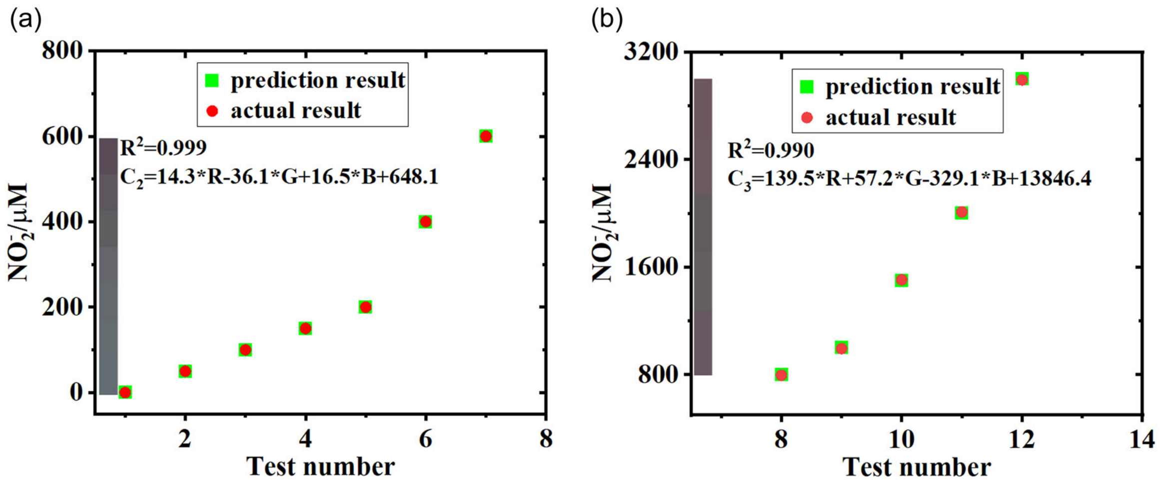

FIGURE 4 Linear fit result comparison. (a) Comparison of prediction and the actual result (0–600 μM). (b) Comparison of prediction and the actual result (800–3000 μM).

performed using RGB values. The fit result is given in Equation (2), and the R^2 is 0.998. As shown in Figure 4a, the prediction results were almost consistent with the actual results.

$$C_2 = 14.3R - 36.1G + 16.5B + 648.1. \qquad (2)$$

③When H was greater than 160 and less than 170, c same multivariate linear fit was conducted. The fit result is given in Equation (3), and the R^2 is 0.990. As shown in Figure 4b, the prediction results were almost consistent with the actual results.

$$C_3 = 139.5R + 57.2G - 329.1B + 13846.4. \qquad (3)$$

④When H was greater than 170, the measurement range was exceeded, and the concentration was set to a maximum value of 3000, as given in Equation (4):

$$C_4 = 3000. \qquad (4)$$

The segment fit result can be summarized as Equation (5):

$$C = \begin{cases} 14.3R - 36.1G + 16.5B + 648.1, \\ \ 100 < H \leq 160 \\ 139.5R + 57.2G - 329.1B + 13846.4, \\ \ 160 < H \leq 170 \\ 0, H \leq 100, or, C < 0 \\ 3000, H > 170 \end{cases}. \qquad (5)$$

Based on Equation (5), we calculated the concentration of each pixel point in the sliced area regardless of the shape size, as shown in Figure 5. The concentration of each point in the actual slice can be obtained after obtaining the scale factor between the pixel size and the actual size of the image, as detailed in Section 2.4.

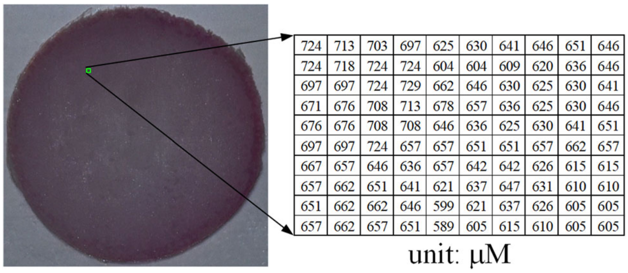

724	713	703	697	625	630	641	646	651	646
724	718	724	724	604	604	609	620	636	646
697	697	724	729	662	646	630	625	630	641
671	676	708	713	678	657	636	625	630	646
676	676	708	708	646	636	625	630	641	651
697	697	724	657	657	651	651	657	662	657
667	657	646	636	657	642	642	626	615	615
657	662	651	641	621	637	647	631	610	610
651	662	662	646	599	621	637	626	605	605
657	662	657	651	589	605	615	610	605	605

unit: μM

FIGURE 5 NO_2^- concentration of each pixel

2.3 | Measurement of penetration depth

In the existing literature, the local penetration depth is observed by metallographic microscopy, and the maximum depth of uneven penetration or the average depth of uniform penetration is measured with high accuracy. However, the cost is high, and the operation is complicated. To deal with this problem, we proposed the use of a digital image method to extract the color-revealing area and simplify the measurement of the penetration depth. The measurement system is shown in Figure 6a. The model tissue was cut vertically along its diameter, and its penetration surface was closely attached to the carrier slide, which effectively ensured the level of the reference surface. The carrier slide was placed on a closed acrylic box with a light source underneath it to effectively distinguish the

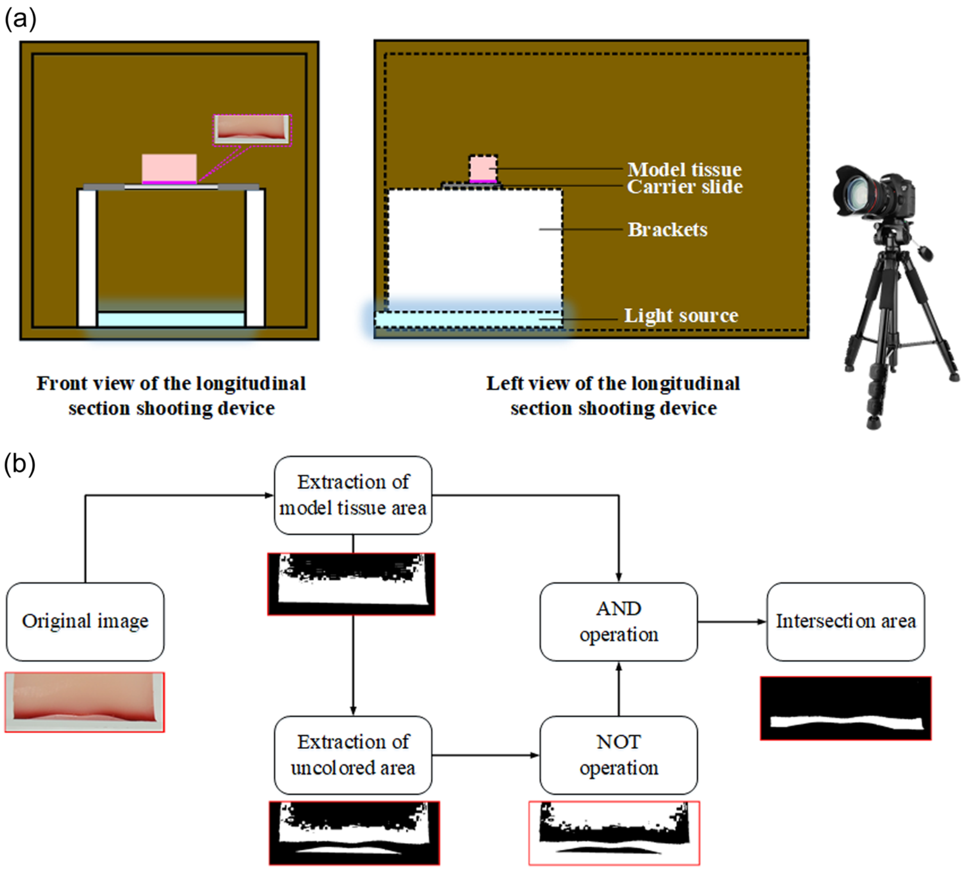

FIGURE 6 Measurement method of penetration depth. (a) Sketch of penetration depth measurement system. (b) Extraction steps of penetration area.

color-revealing area from the noncolor-revealing area. A camera was used to capture longitudinal images for subsequent analyses.

The image extraction of the penetration area was achieved using the steps shown in Figure 6b.

1) Extraction of the model tissue area: map the original RGB image to the HSV space, and extract the *mask* whose HSV pixel values are contained in {[0,43,46], [10,255,255]} and {[156,43,46], [180,255,255]} according to the color feature.
2) Extraction of uncolored area: Convert the RGB image of the *mask* area into a gray image, and perform a binarization operation with a threshold of 127.
3) Math Operation: The NOT operation is performed on the uncolored area image obtained in the previous step and then performs the AND operation with the *mask* to obtain the intersection area.
4) After obtaining the image of the penetration area, count the number of white pixels in each column of the pixel matrix and use the reference size to convert the pixel size into the actual size.

2.4 | Measurement of absolute amount

After obtaining the concentration of each pixel, the absolute amount of NO_2^- penetration in each slice could be obtained by converting the actual size of the slice area, and the derivation formula is given in Equation (6):

$$n = CV = CSh = CS_p n_p h, \tag{6}$$

where n represents the absolute amount of monolayer slice, C is the average concentration of monolayer slice, which can be calculated by Equation (5), S_p is the actual area of each pixel point, n_p is the number of pixel points in the slice area, and h is the slice thickness, which was fixed at 100 μm in this study. S_p is calculated as an example in Figure 7a, which represents the ratio of the actual area of the slice area to the number of pixels in the slice area, as given in Equation (7).

$$S_p = \frac{\pi r^2}{n_{\text{circle}}} \quad . \tag{7}$$
$$r = 10.5\text{mm};\ n_{\text{circle}} = 406744$$

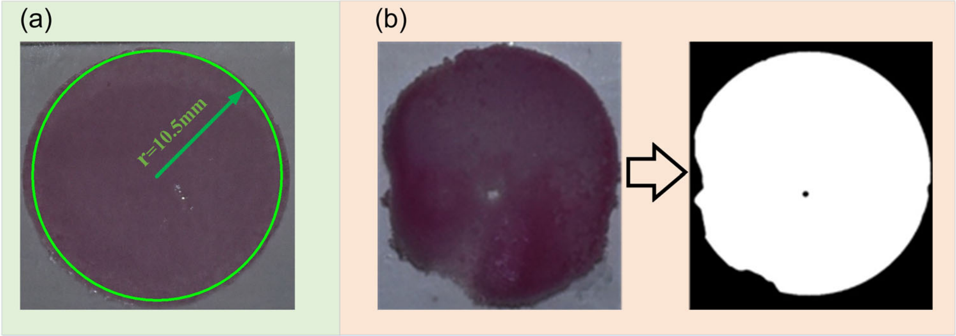

FIGURE 7 (a) S_p calculation example. (b) n calculation example.

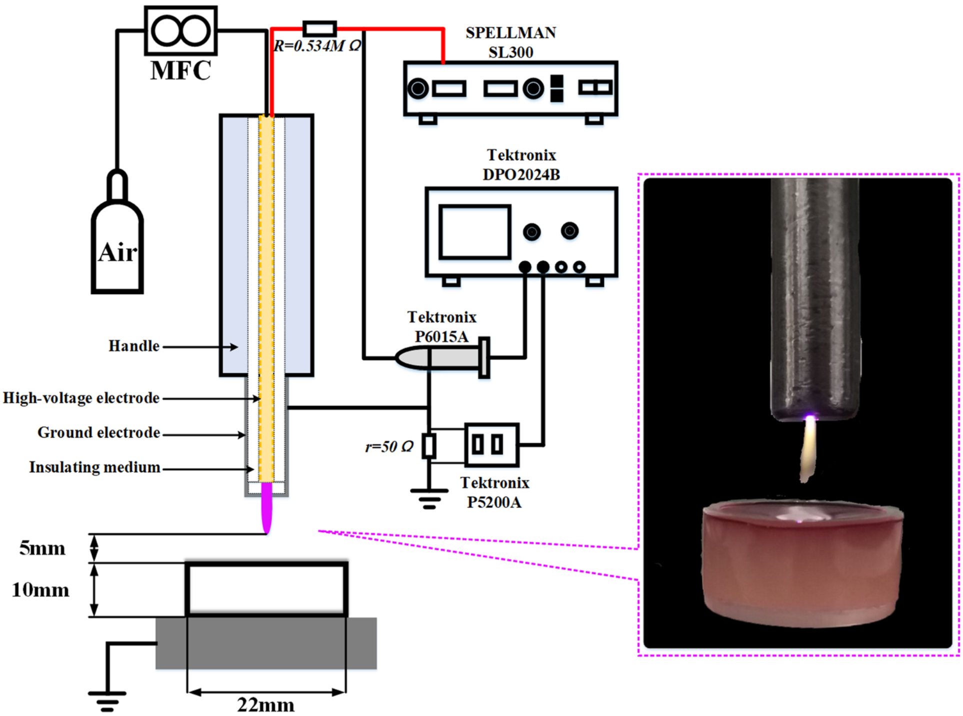

FIGURE 8 Schematic of the plasma jet experimental setup

Here, n is the number of pixels in the slice area that can be obtained based on the extraction of the contour area, regardless of the slice shape. In Figure 7b, for example, the value n is the number of white pixels in the image on the right-hand side. Theoretically, the measurement resolution of this method is 0.03 mm × 0.03 mm.

2.5 | Experimental setup and treatment

Figure 8 shows the schematic of the experimental setup. A plasma jet source includes four parts: a handle, high-voltage electrode, insulating medium, and ground electrode. A high-voltage copper electrode was placed inside a ceramic insulating tube and wrapped with a handle. The stainless-steel ground electrode was mounted outside the ceramic tube with a 0.8-mm diameter hole for gas flow and plasma out. A DC power supply (Spellman SL300) was used, and the amplitude of the applied voltage was fixed at 5 kV. A 0.534 MΩ resistor R and a 50 Ω current-sampling resistor r were connected in series in the circuit. During the treatment, the preprepared sample was placed inside a Petri dish. Due to the size limitation of the freezing microtome, the petri dish was 22 mm in diameter and 10 mm in height, and the model tissue filled the petri dish. The end of the jet was 5 mm from the sample surface, and the samples were treated with the plasma jet for 1, 2, and 3 min at flow rates of 1.0, 1.5, and 2.0 standard liter per minute (SLM), respectively.

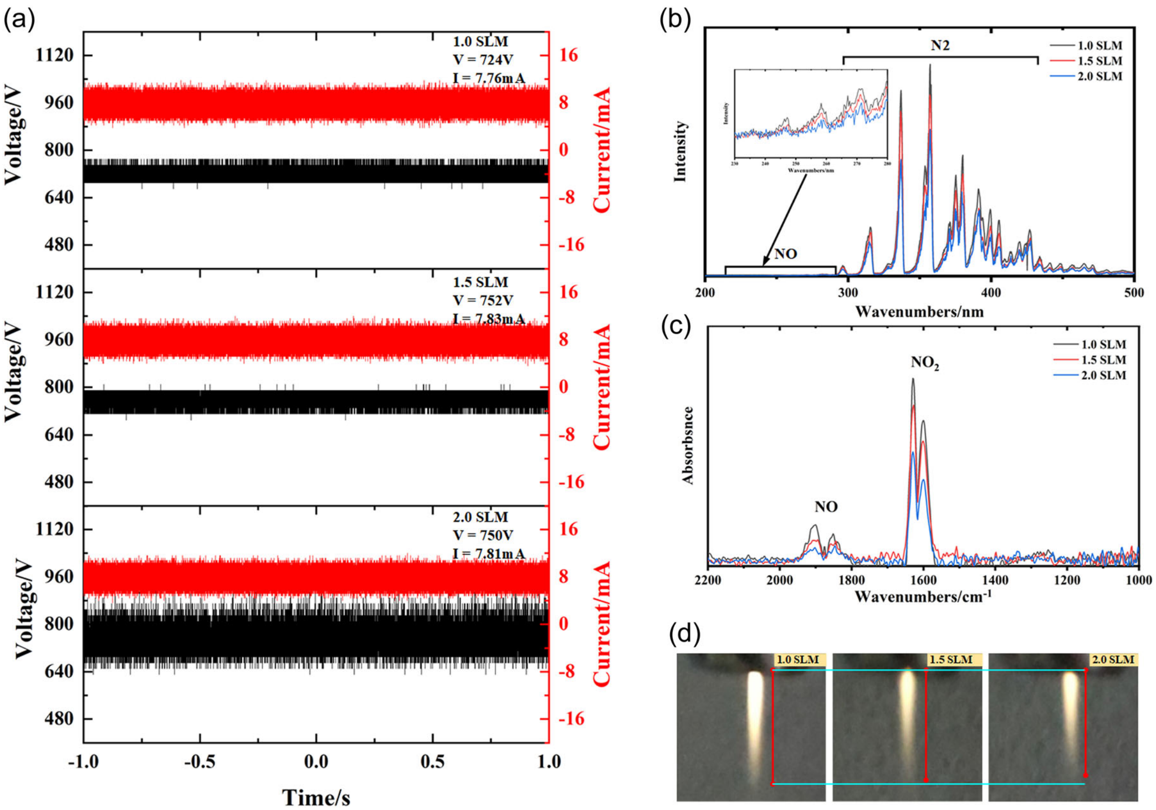

FIGURE 9 (a) Voltage and current waveform of the plasma jet. (b) Optical emission spectrum. (c) FTIR spectrum of gas phase products. (d) Length of the plasma jet.

The emission spectrum of the plasma jet was measured using an emission spectrometer (SR-500I-A; Andor). During the measurement, the distance from the optical fiber outlet of the emission spectrometer to the plasma jet was 2 cm, and the optical fiber outlet was coaxial with the jet. The gas-phase product was introduced into a gas cell and detected by Fourier transform infrared (FTIR) spectroscopy (BRUKER, VERTEX70).

3 | RESULTS AND DISCUSSION

3.1 | V-I characteristic and gas phase products

Typical waveforms of the plasma jet with different flow rate are shown in Figure 9a, where the input voltage was 5 kV. The discharge voltage fluctuated slightly at approximately DC 720–750 V with the flow rate during stable operation, and the current was approximately DC 7.8 mA. The power consumption was approximately 5.6–5.8 W. The average values of voltage, current, and power tended to increase very slightly with the flow rate. In particular, when the flow rate was 1.5 SLM and 2 SLM, the average values were approximately the same, but the voltage fluctuation increased.

Figure 9b shows the emission spectrum of the plasma jet with different flow rate. It was found that most of the spectral lines were concentrated within 200–500 nm, and the main products were NO (200–280 nm) and the N_2 second positive system (300–500 nm). Figure 9c shows the FTIR spectrum of the gas-phase product with different flow rates. It could be observed that the discharge products were mainly NO (around 1800 cm^{-1}) and NO_2 (1550–1675 cm^{-1}), and no ozone O_3 was produced. When the gas-phase products interact with the model tissue, NO_2^- is generated. The intensity and absorbance values of both the emission and FTIR spectra decreased with increasing flow rate, which indicated that the concentration of the corresponding species decreased with increasing flow rate. This phenomenon may be attributed to several factors. As shown in Figure 9d, the length of the jet decreased with increasing flow rate, which may be related to the Reynolds number at the outlet. The Reynolds numbers at the outlet for the flow rates of 1.0 SLM, 1.5 SLM, and 2.0 SLM were 1756, 2634, and 3512, respectively, which correspond, respectively, to the laminar flow state, transition state to turbulent flow, and transition state to turbulent flow. During the

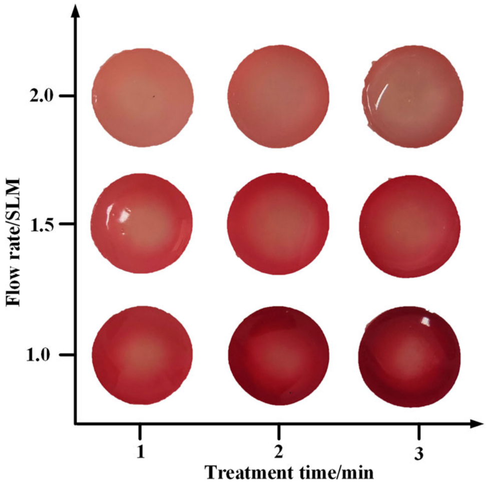

FIGURE 10 Images of plasma treated model tissue versus treatment time and flow rate

experiment, the jet could not be stably maintained in the transition state in a single shape. These factors may have led to the decrease in the efficiency of generation and utilization of the active species.

3.2 | Images of treated model tissue under different conditions

Images of the treated model tissues under different conditions are shown in Figure 10. The treatment times were 1, 2, and 3 min, and the gas flow rates were 1, 1.5, and 2 SLM. It can be observed that the surface color of the model tissue after treatment shows the characteristics of light in the middle and dark in the periphery, especially under the low flow rate treatment. Visually, under the same treatment time, as the flow rate increased, the overall color became lighter. Under the same flow rate, the overall color became darker as the treatment time increased. This phenomenon may be explained as follows: owing to the distribution of the flow velocity field, the larger velocity is in the middle region and the smaller velocity is around, which blows the RNOS to the surrounding region. A similar distribution has been reported in Nie et al.[19]

However, bare eyes can only indicate the color nuances between different samples. The color distribution and depth of penetration were directly related to the NO_2^- concentration and total amount. Therefore, the concentration distribution of each layer and depth was quantitatively analyzed using the proposed method in the following sections.

3.3 | Cross-sectional concentration distribution

After obtaining the image of the slice region, the concentration value of each pixel point was obtained using Equation (5). As shown in Figure 11a, multiple concentration distribution maps depict the NO_2^- spatial distribution in the model tissue after plasma treatment. Layers 4, 8, 12, 16, and 20 are shown with a treatment time of 1 min and a flow rate of 1.0 SLM. For the monolayer slice, a ring structure with a light color in the middle and a dark color around is presented, and the corresponding concentration is low in the middle and high around, which is consistent with the surface color distribution features in Figure 10. The NO_2^- concentration in the middle region varied in the range of 0–500 μM, and the concentration in the surrounding region varied from 200 to 1800 μM. The concentration difference between the middle and surrounding areas decreased significantly with an increase in the penetration layer. This suggests that the nonuniform RNS distribution leads to nonuniform NO_2^- penetration under the action of the gas velocity field, and the limited Petri dish boundary intensifies this effect. As the effect of the velocity field decreased in the deep layer, the concentration distribution gradually became uniform.

As the penetration depth increased, the average concentration of NO_2^- decreased, as expected. Figure 11b,c shows the average concentration of each layer versus the flow rate and treatment time. It can be observed that the average concentration of each layer gradually decreases with increasing penetration depth. Under the same treatment time, the overall concentration in the low-flow-rate group was higher than that in the high-flow-rate group. This involved two effects: on the one hand, from the perspective of the gas phase products, as the flow rate increased, the efficiency of the generation of active species decreased and the number of active species in contact with the model tissue with same treatment time may not increase. On the other hand, when the gas flow rate was slower, the gas-phase products had more time to react with the model tissue and cause more NO_2^- to penetrate the tissue. Under the same flow rate, the concentration in the shallow layer had nearly no difference and became higher in the deeper layer as the treatment time increased. This is because the long treatment time results in the accumulation of more RNOS in the tissue, which could penetrate deeper into the layer. The average concentration of osmotic NO_2^- in the treated model tissue was approximately 500 μM, and the penetration concentration in each layer was between 0 and 1400 μM. Compared with

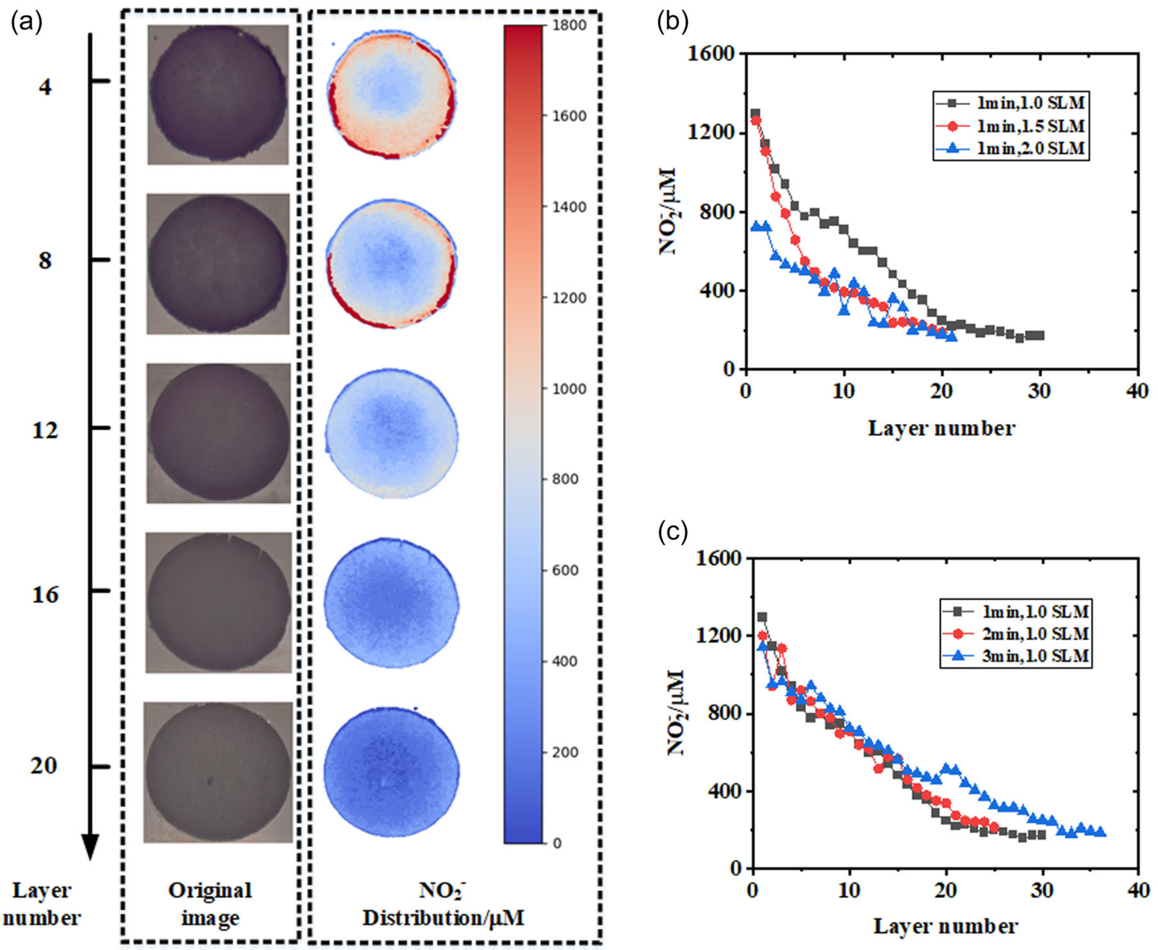

FIGURE 11 Cross-sectional concentration distribution. (a) NO_2^- distribution of layers 4, 8, 12, 16, 20 at 1 min, 1.0 SLM. (b) Average concentration with layer number at 1 min 1.0 SLM, 1.5 SLM, 2.0 SLM. (c) Average concentration with layer number at 1.0 SLM 1 min, 2 min, 3 min. SLM, standard liter per minute.

the maximum average concentration of NO_2^- of 290 μM using mouse skin treated by He+O_2 plasma jet[20] and 600 μM using 2% gelatin solution treated by APPJ or kINPen,[31] the average concentration of 500 μM obtained in this study was of the same order of magnitude. Considering the different plasma jet sources and biological tissue models used, the differences in concentration values were acceptable.

3.4 | Penetration depth

The image and distribution curve of the penetration depth in the longitudinal section versus the flow rate are shown in Figure 12. The curve exhibited a parabolic trend, which is consistent with the aforementioned analysis of the effect of the airflow field on the RNOS distribution. Under the action of airflow, the velocity in the middle area is large, the surrounding velocity is smaller, and the airflow blows the RNS to the surrounding area, resulting in deeper penetration and higher concentration in the surrounding area, as well as shallow penetration and lower concentration in the middle area. Simultaneously, it could be found that with a low flow rate, the penetration of the model tissue is deeper, which is also consistent with the concentration variation with the number of layers. The maximum penetration depth could reach approximately 1.6 mm at the edge (1 min, 1.0SLM) and a minimum of 0.4 mm at the center (1 min, 2.0 SLM). In the existing literature, the measured penetration depth of NO_2^- in pig muscle tissue under plasma jet treatment was between 0.5 and 1.5 mm,[19] and the penetration depth of NO_2^- in 15% gelatin treated by surface air discharge was between 0.5 and 2 mm.[18] The penetration depth in the radial direction in our measurement was in the range of 0.4–1.6 mm, which was in the same range as that of previously reported results. The RNS has a stronger penetration ability than ROS [16,17] and plays a major role in medical applications.

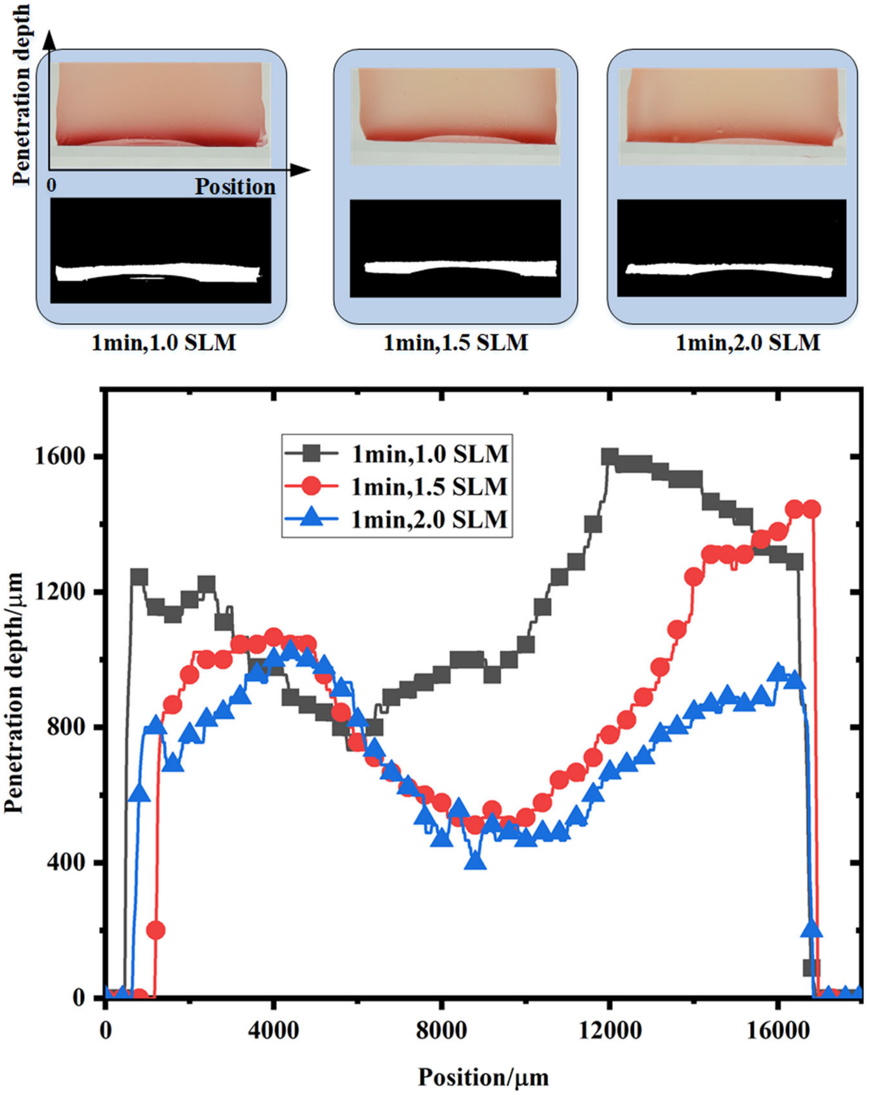

FIGURE 12 Distribution of penetration depth in the longitudinal section at 1 min and 1.0 standard liter per minute (SLM), 1.5 SLM, 2.0 SLM

3.5 | Absolute penetration amount

As shown in Figure 13a, after obtaining the NO_2^- concentration at each point in each layer, the absolute amount of each layer can be obtained according to Equation (6). The penetration amount of each layer can reach up to 0.01 μmol. Subsequently, the total NO_2^- penetration amount in the whole model tissue was obtained by summing up the penetration amount of each layer. The results of the absolute amount versus treatment time and flow rate are shown in Figure 13b. The total amount increased with treatment time and decreased with increasing flow rate. The highest amount is 0.55 μmol in the 3 min and 1.0 SLM treatment group, while the lowest amount is in the 1 min and 2.0 SLM treatment group. As mentioned above, on the one hand, from the spectrum results, the gas-phase product yield decreased with increasing flow rate, which did not always increase the penetration amount in the group with higher flow rates. On the other hand, the longer treatment allows more contact with the tissue and accumulates more species in the tissue; on the contrary, the large flow rate reduces the contact time with the tissue and lowers the amount of species accumulation.

3.6 | Effects of interference factors

Owing to the complex physical and chemical reactions involved in the process of plasma-treating of model tissue, many interference terms may be expected to emerge during NO_2^- concentration measurement, such as ROS, nitrification, and dimple deformation.

For the influence of ROS, we consider the following factors. First, these ROS do not directly react with Griess to affect the color reaction. Second, because there was a 5 cm gap between the plasma jet end and the surface of the model tissue, the short-lived O, OH, and so on, were not considered in terms of their effect on penetration, especially in the deep layer. Third, as for a long-lived

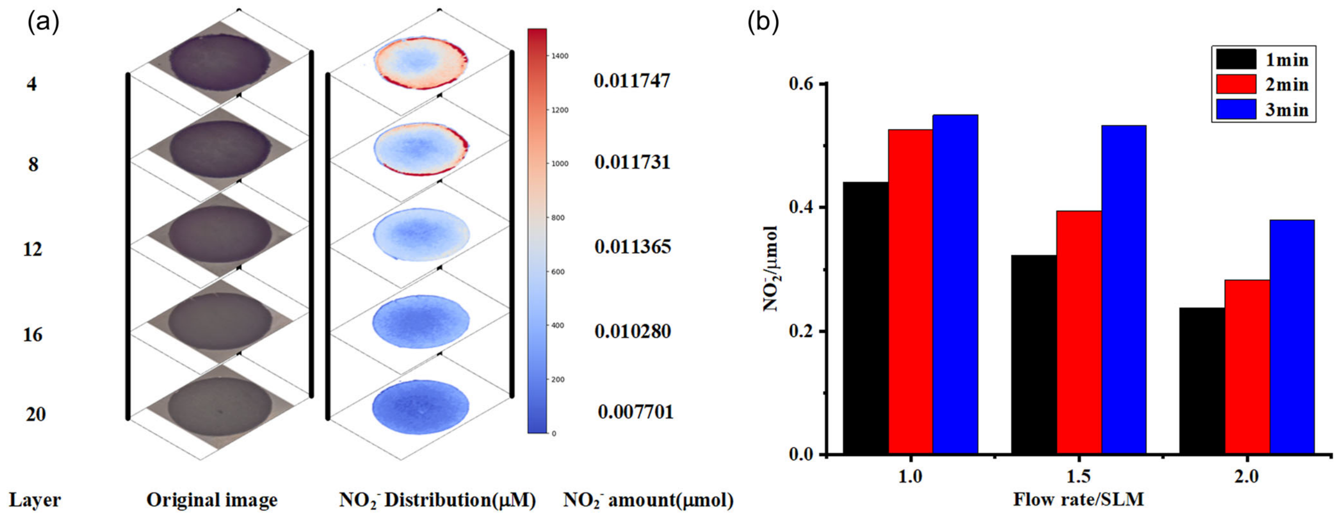

FIGURE 13 Absolute amount for plasma jet. (a) Calculation and accumulation of absolute amount. (b) Comparison of the absolute amount of permeation at a flow rate of 1.0, 1.5 SLM for 1, 2, and 3 min. SLM, standard liter per minute.

species H_2O_2, because gelatin inhibits the fluidity relative to the solution, the reaction that consumes H_2O_2 and NO_2^- was slowed down. This resulted in better stability of the permeated RONS, and stable concentration values were observed over several hours.[31]

The issue of NO_2 reacting with Griess has been reported in the literature.[32,33] Because Griess contains aromatic ring components, the nitration of NO_2 consumes part of the Griess through the following reaction path without producing a color reaction.[33] However, nitrification was only dominant at high concentrations of NO_2, and its effects at low concentrations were very small.[33] To estimate the concentration levels of NOx and Griess, a NOx detector (HD-P900) was used to detect the NOx concentration generated at three different flow rates near the jet outlet, and the maximum value was approximately 6 μmol/L. This was a rough estimation test; however, the obtained value was far less than the Griess concentration of 4000 μmol/L. Hence, we considered that the nitrification of NO_2 exhibited negligible effects on the overall results in this case.

Under the action of gas flow, dimples appear on the soft surface, which may lead to a change in the surface velocity distribution, thereby affecting the NO_2^- distribution. To investigate the effect of dimples on the variations in distribution between the middle and surrounding areas, we premade different sizes of dimples on the surface of the gelatin. Samples named dimple 0 (no dimple), dimple 1 (a small dimple with a depth of 0.25 mm and diameter of 3 mm), dimple 2 (a medium dimple with a depth of 0.33 mm and diameter of 5.8 mm), dimple 3 (a large dimple with a depth of 0.83 mm and diameter of 7.6 mm) were tested under the treatment condition of 1.5 SLM for 1 min. We characterized the penetration distribution from the perspective of the penetration depth as shown in Figure 14. We found that the distribution characteristics of shallow penetration in the middle area and strong penetration in the surrounding area remained under the condition of different degrees of dimples.

From the perspective of flow field distribution, for the issue of dimples generated by such a plasma jet, the characteristics of the flow field have a strong relationship with the relative depth. The depth δ of the dimples measured in our experiment was mostly less than 1 mm, and the diameter D of the dimple area was ~10 mm. The relative depth δ/D was less than or equal to 0.1. When δ/D was less than or equal to 0.1, the dimples had negligible effects on the flow pattern, which is similar to the smooth flow results in Xie et al.[34] Hence, the dimple shape exhibited relatively insignificant effects on the penetration characteristics of the middle and surrounding areas. Further research remains necessary to study the effect of the flow field on the distribution of the concentration.

3.7 | Comparison with other methods

Most measurement methods for existing reactive species in tissues do not offer direct quantitative measurements of the concentration. Although UV-Vis spectroscopy can measure reactive species components in a model tissue, it can only obtain absorbance on a two-dimensional plane and qualitatively analyze relative concentrations. If calibration is conducted before measurements, quantitative results may also be obtained. However, for a model tissue with nonuniform penetration after plasma jet

FIGURE 14 Effect of dimples on the distribution of penetration depth

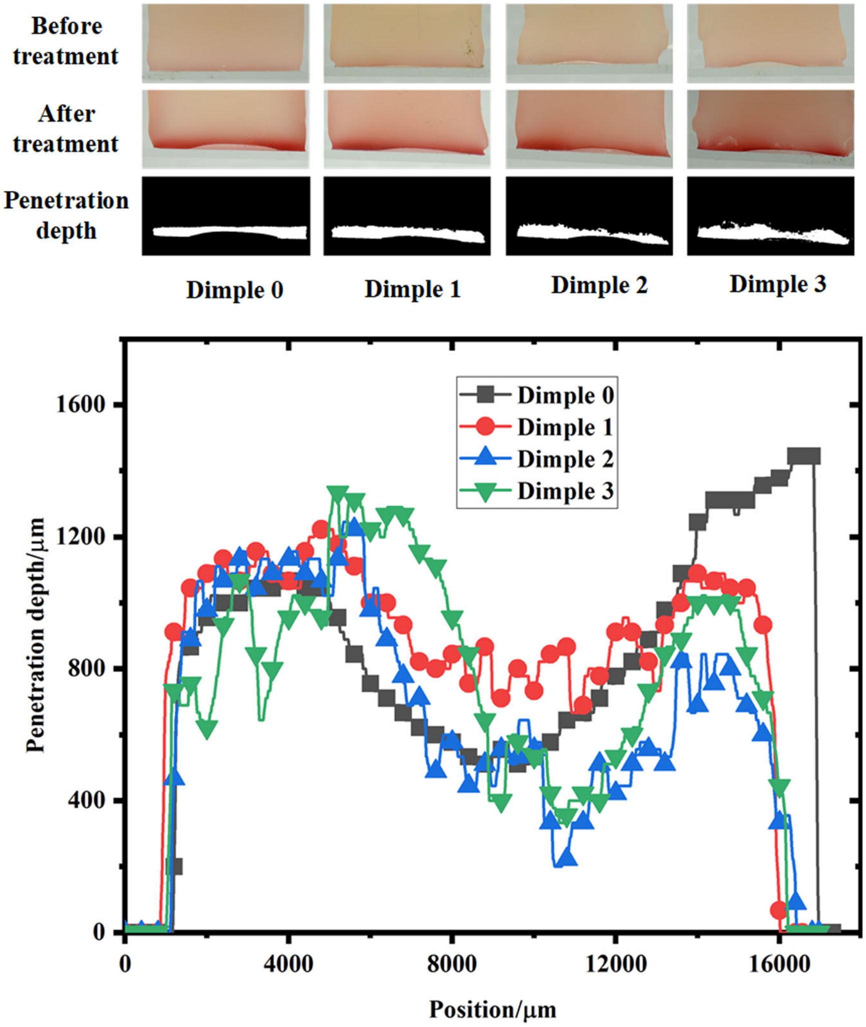

treatment, as in this study, it is impossible to accurately measure the absolute concentration of each point using UV-Vis spectroscopy because of the limitation of the beam area. In addition, the measurement of spatial distribution by UV-Vis must be performed by moving the tissue slice around to measure the whole slice, which is inefficient and difficult to perform.

The measurement method proposed in this study can quickly obtain the concentration of each point of the entire layer and is not affected by the sample shape and uniformity. The proposed method is low cost, fast, and smart. Light interference in image processing may be one of the issues; however, this can be improved by fixing the light source and performing multiple measurements.

4 | CONCLUSION

In this study, we proposed a method based on image processing technology to investigate the spatial distribution and total amount of reactive species inside a plasma-treated model tissue. The quantitative concentration of NO_2^- for each pixel in the sample slice was obtained, along with the penetration depth. The quantitative spatial distribution *versus* treatment time and the flow rate were compared, and it was found that the average concentration increased with the treatment time and decreased with the flow rate. The concentration in the middle area was lower than that in the surrounding area in each sliced layer, and became uniform with an increase in the layer number. In the longitudinal section of the model tissue, the penetration depth exhibited a parabolic change in the radial direction. The total NO_2^- amount inside the treated model tissue reached up to 0.55 μmol in the 3 min and 1 SLM treatment group. It showed a positive correlation with treatment time and a negative correlation with the flow rate. The airflow field may have been the main contributor to this phenomenon.

The proposed method could realize high-resolution quantitative measurements of spatial-temporal distribution and the total amount of reactive species inside the treated tissue and offers a new method for fast and smart measurement in plasma medicine.

ACKNOWLEDGEMENT

The authors are grateful for financial support from the National Natural Science Foundation of China (No. 51907076) and Institute of Environmental Health, Wuhan Center for Disease Control and Prevention.

DATA AVAILABILITY STATEMENT

Data available on request from the authors.

ORCID

Zilan Xiong http://orcid.org/0000-0003-1095-3959

REFERENCES

[1] Z. Xiong, J. Roe, T. C. Grammer, D. B. Graves, *Plasma. Process. Polym.* **2016**, *13*(6), 588. https://doi.org/10.1002/ppap.201600010

[2] Z. Xiong, D. B. Graves, *J. Phys. D. Appl. Phys.* **2017**, *50*(5), 05LT01. https://doi.org/10.1088/1361-6463/50/5/05LT01

[3] Z. Xiong, R. Huang, Y. Zhu, K. Luo, M. Li, Z. Zou, R. Han, *Plasma. Process. Polym.* **2021**, *18*(5), 1. https://doi.org/10.1002/ppap.202000204

[4] J. Y. Jang, Y. J. Hong, J. Lim, J. S. Choi, E. H. Choi, S. Kang, H. Rhim, *Biomaterials* **2018**, *156*, 258. https://doi.org/10.1016/j.biomaterials.2017.11.045

[5] D. B. Graves, *J. Phys. D. Appl. Phys.* **2012**, *45*(26), 263001. https://doi.org/10.1088/0022-3727/45/26/263001

[6] E. J. Szili, S. H. Hong, J. S. Oh, N. Gaur, R. D. Short, *Trends Biotechnol.* **2018**, *36*(6), 594. https://doi.org/10.1016/j.tibtech.2017.07.012

[7] D. Dobrynin, G. Fridman, G. Friedman, A. Fridman, *Plasma Med.* **2012**, *2*(1–3), 71. https://doi.org/10.1615/PlasmaMed.2013006218

[8] J. S. Oh, E. J. Szili, N. Gaur, S. H. Hong, H. Furuta, H. Kurita, A. Mizuno, A. Hatta, R. D. Short, *J. Phys. D. Appl. Phys.* **2016**, *49*(30), 304005. https://doi.org/10.1088/0022-3727/49/30/304005

[9] A. V. Omran, G. Busco, S. Dozias, C. Grillon, J. Pouvesle, E. Robert, *24th Int. Symp. Plasma Chem.* **2019**, 1. https://hal.archives-ouvertes.fr/hal-02263879

[10] E. J. Szili, J. W. Bradley, R. D. Short, *J. Phys. D. Appl. Phys.* **2014**, *47*(15), 152002. https://doi.org/10.1088/0022-3727/47/15/152002

[11] T. Kawasaki, W. Eto, M. Hamada, Y. Wakabayashi, Y. Abe, K. Kihara, *Jpn. J. Appl. Phys.* **2015**, *54*(8), 086201. https://doi.org/10.7567/JJAP.54.086201

[12] T. Kawasaki, G. Kuroeda, R. Sei, M. Yamaguchi, R. Yoshinaga, R. Yamashita, H. Tasaki, K. Koga, M. Shiratani, *Jpn. J. Appl. Phys.* **2018**, *57*(1), 01AG01. https://doi.org/10.7567/JJAP.57.01AG01

[13] T. Kawasaki, F. Mitsugi, K. Koga, M. Shiratani, *J. Appl. Phys.* **2019**, *125*(21), 213303. https://doi.org/10.1063/1.5091740

[14] A. Nakajima, G. Uchida, T. Kawasaki, K. Koga, T. Sarinont, T. Amano, K. Takenaka, M. Shiratani, Y. Setsuhara, *J. Appl. Phys.* **2015**, *118*(4), 043301. https://doi.org/10.1063/1.4927217

[15] T. Kawasaki, K. Kawano, H. Mizoguchi, Y. Yano, K. Yamashita, M. Sakai, T. Shimizu, G. Uchida, K. Koga, M. Shiratani, *IEEE Trans. Plasma Sci.* **2014**, *42*(10), 2482. https://doi.org/10.1109/TPS.2014.2325038

[16] T. He, D. Liu, Z. Liu, S. Wang, Z. Liu, M. Rong, M. G. Kong, *J. Phys. D. Appl. Phys.* **2019**, *52*(4), 045204. https://doi.org/10.1088/1361-6463/aaed6f

[17] D. Liu, T. He, Z. Liu, S. Wang, Z. Liu, M. Rong, M. G. Kong, *Plasma. Process. Polym.* **2018**, *15*(10), 1800057. https://doi.org/10.1002/ppap.201800057

[18] T. He, D. Liu, H. Xu, Z. Liu, D. Xu, D. Li, Q. Li, M. Rong, M. G. Kong, *J. Phys. D. Appl. Phys.* **2016**, *49*(20), 205204. https://doi.org/10.1088/0022-3727/49/20/205204

[19] L. Nie, Y. Yang, J. Duan, F. Sun, X. Lu, G. He, *J. Phys. D. Appl. Phys.* **2018**, *51*(34), 345204. https://doi.org/10.1088/1361-6463/aad427

[20] J. Duan, L. Gan, L. Nie, F. Sun, X. Lu, G. He, *Phys. Plasmas* **2019**, *26*(4), 043504. https://doi.org/10.1063/1.5082160

[21] J. Duan, X. Lu, G. He, *Phys. Plasmas* **2017**, *24*(7), 073506. https://doi.org/10.1063/1.4990554

[22] K. Nakano, R. Hirofuji, T. Ohnishi, M. Hauta-Kasari, I. Nishidate, H. Haneishi, *IEEE Access.* **2019**, *7*, 56469. https://doi.org/10.1109/ACCESS.2019.2913878

[23] Y. Wang, Q. Ye, Z. Guo, *IEEE Trans. Plasma Sci.* **2021**, *49*(5), 1574. https://doi.org/10.1109/TPS.2021.3073175

[24] Z. Yuan, Q. Ye, Y. Wang, Z. Guo, *IEEE Trans. Instrum. Meas.* **2021**, *70*, 1. https://doi.org/10.1109/TIM.2020.3031543

[25] Z. Yuan, Q. Ye, Y. Wang, H. Shi, *IEEE Trans. Instrum. Meas.* **2021**, *70*(19), 21221. https://doi.org/10.1109/TIM.2021.3112003

[26] C. Lu, Z. Xiong, *Plasma Process. Polym.* **2022**, *19*, 1. https://doi.org/10.1002/ppap.202100205

[27] Z. Zou, R. Han, C. Lu, Z. Xiong, *Plasma. Process. Polym.* **2021**, *18*(1), 1. https://doi.org/10.1002/ppap.202000139

[28] S. Afewerki, A. Sheikhi, S. Kannan, S. Ahadian, A. Khademhosseini, *Bioeng. Transl. Med.* **2019**, *4*(1), 96. https://doi.org/10.1002/btm2.10124

[29] Q. Mao, O. Hoffmann, K. Yu, F. Lu, G. Lan, F. Dai, S. Shang, R. Xie, *Mater. Des.* **2020**, *194*, 108916. https://doi.org/10.1016/j.matdes.2020.108916

[30] J. Sun, X. Zhang, M. Broderick, H. Fein, W. P. Instruments, S. International, *Sensors* **2003**, *3*, 276. http://www.mdpi.net/sensors

[31] C. Labay, M. Roldán, F. Tampieri, A. Stancampiano, P. E. Bocanegra, M. P. Ginebra, C. Canal, *ACS Appl. Mater. Interfaces* **2020**, *12*(42), 47256. https://doi.org/10.1021/acsami.0c12930

[32] B. E. Saltzman, *Anal. Chem.* **1954**, *26*(12), 1949. https://doi.org/10.1021/ac60096a025

[33] I. C. Huygen, *Anal. Chem.* **1970**, *42*(3), 407. https://doi.org/10.1021/ac60285a018

[34] Y. Xie, P. Li, J. Lan, D. Zhang, *J. Heat Transfer* **2013**, *135*(5), 1. https://doi.org/10.1115/1.4023360

How to cite this article: B. Wang, H. Wang, Y. Wang, Y. Li, X. Mao, Z. Xiong, *Plasma Process. Polym.* **2022**, e2200066. https://doi.org/10.1002/ppap.202200066